EDGE ARTICLE

Check for updates

Narrowband blue emission with insensitivity to the doping concentration from an oxygen-bridged triarylboron-based TADF emitter: nondoped OLEDs with a high external quantum efficiency up to 21.4%†

Jianmei Han,‡[ab] Zhongyan Huang, ‡[a] Jingsheng Miao,[a] Yuntao Qiu,[a] Ziyang Xie[a] and Chuluo Yang *[a]

Blue thermally activated delayed fluorescence (TADF) emitters that can simultaneously achieve narrowband emission and high efficiency in nondoped organic light-emitting diodes (OLEDs) remain a big challenge. Herein, we successfully design and synthesize two blue TADF emitters by directly incorporating carbazole fragments into an oxygen-bridged triarylboron acceptor. Depending on the linking mode, the two emitters show significantly different photophysical properties. Benefitting from the bulky steric hindrance between the acceptor and terminal pendants, the blue emitter **TDBA-Cz** exhibited a high photoluminescence quantum yield (PLQY) of 88% in neat films and narrowband emission. The corresponding non-doped blue device exhibited a maximum external quantum efficiency (EQE) of 21.4%, with a full width at half maximum (FWHM) of only 45 nm. This compound is the first blue TADF emitter that can concurrently achieve narrow bandwidth and high electroluminescence (EL) efficiency in nondoped blue TADF-OLEDs.

Introduction

Organic light-emitting diodes (OLEDs) are currently one of the competitive candidates for future full-color displays due to their recommendable advantages such as high efficiency, light weight, wide viewing angle and superior mechanical flexibility.[1] Since the pioneering work of Adachi and co-workers reported in 2011, thermally activated delayed fluorescence (TADF) materials without precious heavy metals have been greeted with an avalanche of publicity as the third-generation OLED emitters.[2] The use of metal-free TADF emitters in OLEDs could theoretically achieve 100% internal quantum efficiency by converting electro-generated triplet excitons into singlet excitons *via* an efficient reverse intersystem crossing (RISC) process.[3] Until now, a considerable number of highly efficient TADF-based OLEDs have been successfully reported.[4] Generally, the

commonly adopted design strategy for blue TADF molecules is to construct a donor–acceptor-type (D–A-type) molecular skeleton with strong intramolecular charge-transfer (ICT) character, which inevitably causes broad electroluminescence (EL) spectra with a full width at half maximum (FWHM) of over 80 nm, thereby resulting in inferior color purity and gigantic energy consumption in OLED displays with the use of color filters.[5] To meet the requirements of perfect color purity for practical applications, Lee and coworkers employed the steric hindrance effect to obtain a deep-blue-emitting TADF emitter with a narrow FWHM of 48 nm but with a fairly low external quantum efficiency (EQE) of only 14.0% in 2016.[6] Recently, Hatakeyama and coworkers demonstrated that multi-resonance type TADF molecules composed of a rigid skeleton with an orderly arrangement of boron and nitrogen atoms enabled narrow emission and can be employed to construct highly efficient TADF-OLEDs with high color purity. However, this strategy is only suitable for specially designated molecular frameworks and inapplicable to conventional D–A-type TADF emitters.[7] More importantly, the majority of TADF emitters suffer from serious concentration-caused emission quenching.[4c,8] Consequently, most of the highly efficient TADF OLEDs reported so far can only function well in doped films at low doping concentrations, thereby resulting in complicated manufacturing processes, expensive fabrication, and poor repeatability. To address this drawback, TADF emitters must be

[a]*Shenzhen Key Laboratory of Polymer Science and Technology, College of Materials Science and Engineering, Shenzhen University, Shenzhen 518060, P. R. China. E-mail: clyang@szu.edu.cn*

[b]*College of Physics and Optoelectronic Engineering, Shenzhen University, Shenzhen 518060, P. R. China*

dispersed in a suitable host matrix to alleviate the detrimental quenching. However, the selection of desirable host materials for blue emitters is imperative but is technically difficult because of the limited availability of suitable building blocks. To circumvent this issue, nondoped devices could be adopted to construct highly-efficient TADF OLEDs.

Compared to doped devices, nondoped devices could not only expand the exciton recombination zone but also simplify device fabrication and improve device performance reproducibility due to the unnecessity of precise control of the dopant concentration. Despite these merits, the realization of highly efficient non-doped blue OLEDs with narrowband emission is ever more challenging and needs to be exploited long-term. To the best of our knowledge, up to now, the most efficient non-doped blue-emitting device was reported to have an EQE up to 22.8% but with a slightly broad FWHM of 63 nm.[4b] Therefore, there is a desperate need for the development of new blue TADF emitters which could simultaneously achieve high color purity, high efficiency and low driving voltage for practical applications.

Based on the above considerations, we reported a simple but effective design strategy for constructing highly-efficient TADF emitters with narrowband emission. By directly incorporating two carbazole donors into a rigid oxygen-bridged triarylboron acceptor, a novel TADF emitter was successfully synthesized. Such a structural design strategy not only makes the compound capable of realizing highly-efficient doped blue OLEDs with an EQE up to 31.1% at a doping concentration of 10 wt% but also endows the most efficient narrowband and non-doped blue OLED (EQE up to 21.4%) with an extremely small FWHM of only 45 nm so far.

Results and discussion

The synthetic routes of the designed compound **TDBA-Cz** are depicted in Scheme S1 in the ESI,† which involved the aromatic nucleophilic substitution and Ullmann coupling reaction, followed by the *tert*-butyllithium mediated borylation reactions. For comparison, a reference molecule **DBA-Cz** was rationally designed and synthesized using precursors DBA-2Br and 3,6-di-*tert*-butylcarbazole by the classical coupling method according to the reported literature.[9] Different from **TDBA-Cz**, two carbazole units were introduced into the *meta* position of the boron atom on the other two phenyl rings of the acceptor moiety to elaborate the effect of the substitution site of carbazole units on photophysical characteristics. The chemical structures of all the intermediates and final products were characterized by NMR and high-resolution mass spectroscopy (Fig. S1–S8, ESI†). In addition, as proved by thermogravimetric analysis (TGA, Fig. S9 and S10, ESI†), both **TDBA-Cz** and **DBA-Cz** showed excellent thermal stability with a decomposition temperature (T_d) of 421 and 390 °C at 5% weight loss, respectively.

The design conception is supported by the density functional theory (DFT) and time-dependent DFT (TD-DFT) calculations, as shown in Fig. 1. The detailed computation method is summarized in the ESI.† In the S_0 state, benefitting from the bulky steric hindrance between the donor and acceptor moieties, the two compounds exhibited a distorted molecular configuration with large dihedral angles of over 60°, thereby leading to better spatial separation of the HOMO and LUMO distribution. The LUMO was fully located on the oxygen-bridged triarylboron acceptor unit, while the HOMO was predominantly distributed on the carbazole donor and adjacent benzene ring, and even extended to the acceptor moiety. Such an orbital overlap of the HOMO and LUMO resulted in a slightly enlarged ΔE_{ST} value of 0.23 eV for the two compounds (Fig. 1a and S11†). To further comprehensively understand the excited state properties of **TDBA-Cz** and **DBA-Cz**, the natural transition orbitals (NTOs) for the transition to singlet and triplet excited states
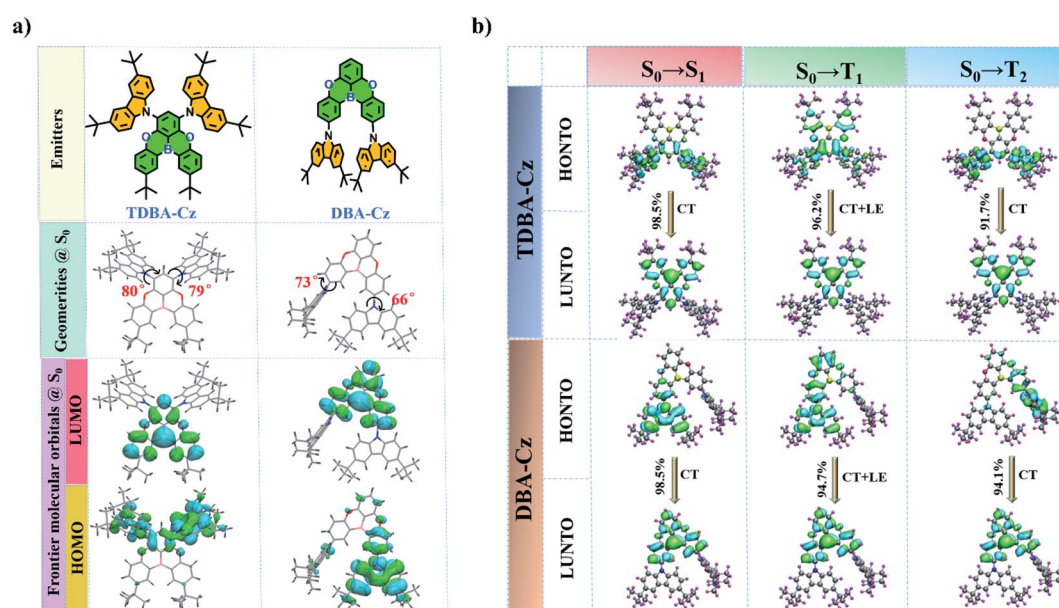

Fig. 1 (a) Molecular structures, optimized ground-state geometries and frontier molecular orbitals of **TDBA-Cz** and **DBA-Cz**. (b) The highest occupied and lowest unoccupied NTOs (HONTO and LUNTO) of **TDBA-Cz** and **DBA-Cz** with the largest contribution.

were examined (Fig. 1b). For $S_0 \rightarrow S_1$ transition, the HONTO and LUNTO of both compounds are similar to their respective HOMO and LUMO of S_0, indicating that singlet emission can be interpreted as charge transfer (CT) emission. While the HONTO of the transition to T_1 is mainly distributed on the carbazole donor and adjacent acceptor moiety, the LUNTO is still fully located on the oxygen-bridged triarylboron unit, suggesting the existence of a mixed transition featuring CT character and locally excited (LE) state character in the triplet state. Such LE characteristics in the triplet state are of vital importance in boosting the RISC process by increasing the spin–orbit coupling (SOC) between the S_1 state with CT characteristics and triplet states. In addition, the transition to T_2 exhibited dominant CT characteristics for both **TDBA-Cz** and **DBA-Cz**, which gave rise to a smaller ΔE_{ST} than that of the T_1 state, so as to facilitate the upconversion of the triplet excitons to the singlet excited state through the RISC process.

The electrochemical properties of both compounds were measured by cyclic voltammetry (CV). As shown in Fig. S12 and S13 in the ESI,† **TDBA-Cz** and **DBA-Cz** exhibited onset oxidation potential values (E_{ox}) of 1.00 and 1.03 eV, respectively. The calculated HOMO energy level (-5.39 eV) of **TDBA-Cz** is about 30 meV lower than that of **DBA-Cz**, which is consistent with the aforementioned DFT calculation results. The preliminary photophysical properties of these two compounds were characterized in dilute toluene solution as illustrated in Fig. 2 and Table 1. Both molecules displayed intense and sharp absorption

bands ranging from 400 to 450 nm, originating from the intramolecular charge transfer (ICT) transitions. The ICT character could be further evidenced by the solvatochromism experiment upon altering the solvent from low polar n-hexene to high polar dichloromethane (DCM). Compared with **DBA-Cz**, **TDBA-Cz** displayed less solvatochromic effect with relatively narrow FWHM as the polarity of the solvent increased, indicating that **TDBA-Cz** possess a bigger contribution from the LE state in higher polar solvent whereas the reverse is true for **DBA-Cz** (Tables S1 and S2, ESI†). In toluene solution, **TDBA-Cz** showed blue emission with a fluorescence spectrum peaking at 461 nm, while **DBA-Cz** showed deep-blue emission with an emission maximum of 447 nm. Importantly, both compounds exhibited narrowband emission with a small FWHM of about 40 nm, which is significantly smaller than those of typical D–A type TADF emitters and even comparable to those of multi-resonance type emitters.[7,10] Furthermore, ΔE_{ST} values were calculated to be 0.14 and 0.03 eV for **TDBA-Cz** and **DBA-Cz** from their respective fluorescence and phosphorescence spectra. Notably, the photoluminescence (PL) spectrum of **DBA-Cz** in neat films exhibited a significant bathochromic-shift and broadened FWHM, while the emission of **TDBA-Cz** closely resembled that of toluene solution. The narrow FWHM for **TDBA-Cz** in different states was mainly attributed to the trivial conformational changes of the molecular structure between the ground state and singlet excited states. As shown in Fig. 3a and b, the molecular geometrical structures of S_0 and S_1 states for these
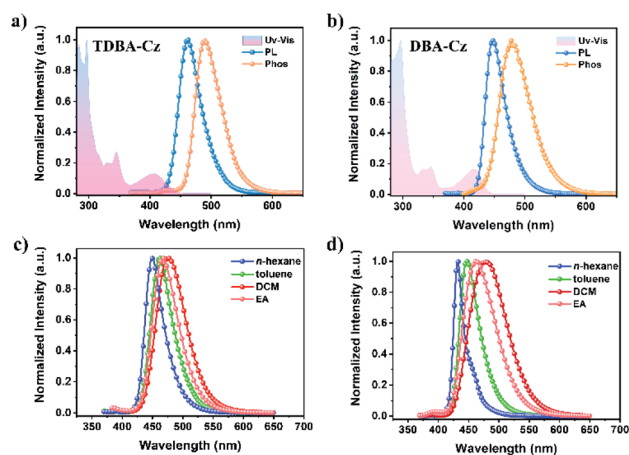

Fig. 2 Normalized UV-vis absorption, fluorescence (298 K) and phosphorescence (77 K) spectra of compounds (a) TDBA-Cz and (b) DBA-Cz in toluene solution (1 × 10^{-5} M). PL spectra of (c) TDBA-Cz and (d) DBA-Cz in different solvents.
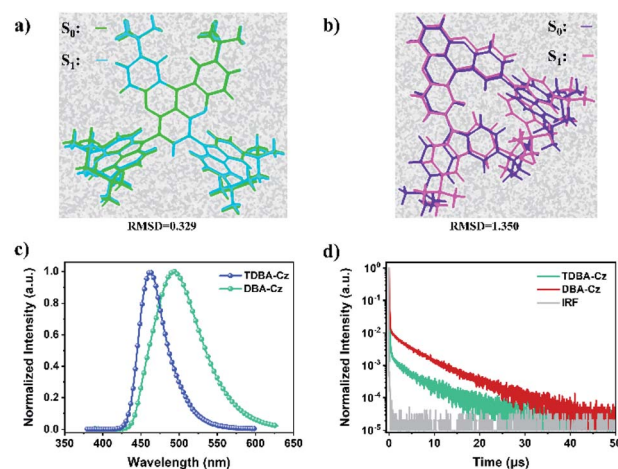

Fig. 3 Calculated RMSD constant between S_0 and S_1 states for (a) TDBA-Cz and (b) DBA-Cz. PL spectra of neat films (c) and transient photoluminescence decay curves (d) of TDBA-Cz and DBA-Cz.

Table 1 Photophysical data of TDBA-Cz and DBA-Cz

Compound	λ_{abs}[a] [nm]	λ_{em}[a] [nm]	FWHM[a] [nm]	E_{S1}[a] [eV]	E_{T1}[a] [eV]	ΔE_{ST}[a] [eV]	τ_{prompt}[b] [ns]	τ_{delay}[b] [µs]	k_r [10^7 s^{-1}]	k_{ISC} [10^8 s^{-1}]	k_{RISC} [10^6 s^{-1}]
TDBA-Cz	406	461	43	2.89	2.75	0.14	7.6	6.1	1.38	1.17	1.40
DBA-Cz	418	447	38	3.00	2.97	0.03	23.7	8.2	0.59	0.31	0.46

[a] Measured in the toluene solution with a concentration of 10^{-5} mol L^{-1}. [b] Measured in neat films of **TDBA-Cz** and **DBA-Cz**.

two molecules were simulated by root mean square deviation (RMSD) to judge the configurational changes of the excited state relative to the ground state. Generally, the structural variations between S_0 and S_1 are closely related to the FWHMs of the emission spectra. As for **TDBA-Cz**, the major discrepancy between S_0 and S_1 states is the slightly twisted vibrations of the noncoplanar tertiary butyl moieties, with a small average alteration in configuration of 0.329 Å. However **DBA-Cz** exhibited significant changes not only in the rigid oxygen-bridged triarylboron acceptor but also in carbazole donors between S_0 and S_1 states of molecular conformation, thereby resulting in an immense average RMSD value of up to 1.35 Å. The above results indicated that the introduction of two carbazole units to the same phenyl ring of the boron-based core could effectively suppress the molecular configuration relaxation of the radiative transition process, thus obtaining narrowband emissions benefiting from small structural changes.

To factually assess the performance of **TDBA-Cz** and **DBA-Cz** as TADF emitters, photophysical properties of doped thin films were recorded using bis[2-(diphenylphosphino)phenyl]ether oxide (DPEPO) as the host material. As depicted in Fig. S14 and S15,† both doped films (dopant concentration of 10 wt%) gave blue emissions peaking at 456 nm and 450 nm with corresponding FWHMs of 46 nm and 47 nm for **TDBA-Cz** and **DBA-Cz**, respectively. In addition, on increasing the doping concentration of **TDBA-Cz** in the DPEPO host, a slight change of the spectral redshift with FWHM narrowing was observed, with an emission peak wavelength ranging from 456 (FWHM: 46 nm) to 462 nm (FWHM: 41 nm) when going from 10 to 100 wt% (Table S3†). Notably, the films possess high PLQYs, which gradually reduce from 100% at a 10 wt% concentration to 88% in the neat film. The high PLQYs confirmed the good suppression of aggregation-caused quenching achieved by rational molecular design, further elucidating potentiality for the fabrication of non-doped OLEDs. In contrast, **DBA-Cz** displayed a substantial spectral redshift of the emission (450–494 nm) and broadened FWHM (47–82 nm) in DPEPO blends as the doping concentration increased (Fig. S15†), accompanied by a significant PLQY drop from 90% in the 10 wt% DPEPO blends to 52% in the neat film (Fig. S16 and Table S4, ESI†). To further elucidate the TADF nature of these compounds, temperature-dependent transient PL decay curves in thin films were measured. The detailed rate constants including the radiative decay rate constant (k_r), intersystem crossing rate constant (k_{ISC}) and RISC rate constant (k_{RISC}) were also calculated according to the references, and summarized in Table 1. As shown in Fig. 3d, both **TDBA-Cz** and **DBA-Cz** in neat films exhibited typical TADF features with nanosecond-order prompt decays and microsecond-order delayed decays. Moreover, the fluorescence decay was sensitive to temperature, and the intensity of the delayed fluorescence component increased with the temperature increase from 77 to 300 K (Fig. S17, ESI†), thus proving the TADF characteristics of both emitters. Remarkably, the delayed fluorescence lifetime (τ_d) of **TDBA-Cz** was 1.3 times shorter than that of **DBA-Cz** (8.2 μs), which mostly benefits from the fast ISC and RISC process of **TDBA-Cz** in films. In addition, combined with large rate constants of fluorescence (k_F: 1.37×10^7 s^{-1}), concentration quenching of triplet excitons in electroluminescent devices could be efficiently alleviated thereby suppressing efficiency roll-off with increasing luminance. However, **DBA-Cz** showed relatively small k_{ISC}, k_F and k_{RISC} values, which were one order of magnitude less than those of **TDBA-Cz**. According to Fermi's golden rule, k_{RISC} is proportional to the SOC constant between the singlet and triplet states and inversely proportional to the energy difference ΔE_{ST}.[3c,4b,11] The computed SOC value $\langle S_1|H_{SOC}|T_1\rangle$ (0.336 cm^{-1}) of **DBA-Cz** is much greater than $\langle S_1|H_{SOC}|T_2\rangle$ (0.018 cm^{-1}), indicating that the RISC process was dominated by the transition from the T_1 state to the S_1 state. In comparison, **TDBA-Cz** with a larger ΔE_{ST} value and shorter decay lifetime was found to afford a slightly smaller $\langle S_1|H_{SOC}|T_1\rangle$ of 0.218 cm^{-1} than **DBA-Cz**, unambiguously indicating that other electronic transition states are involved in the triplet-singlet spin conversion process to accelerate RISC. The further analysis of the NTO proclaimed that the T_2 triplet state below the S_1 energy level was found to afford a fairly large SOC with its S_1 state ($\langle S_1|H_{SOC}|T_2\rangle$ of 0.917 cm^{-1}) compared to its T_1 counterpart. Therefore, **TDBA-Cz** is expected to undergo a more efficient RISC process through the interstate coupling with the T_2 state.

To better understand the configuration of **TDBA-Cz**, its single crystal was cultivated by slow evaporation of ethyl acetate solvent at room temperature. As indicated in Fig. S18 in the ESI,† the crystal was monoclinic with space group $P2_1/c$. Due to the steric hindrance between the two bulky carbazole groups, the acceptor moiety was slightly distorted out of plane, as shown by its side view in Fig. S18,† with a dihedral angle of 14.39° between the two wing phenyl rings (B/B′). In addition, the dihedral angles between the two carbazole units and the adjacent phenyl ring are 88.76° (A/D) and 58.71° (A/D′), respectively. Such highly twisted configuration implied that the concentration-caused emission quenching could be effectively suppressed. Notably, the twisted conformation prevents the molecules from forming detrimental π···π intermolecular interactions. Only weak intermolecular interactions, including CH···π (2.768 Å, 2.813 Å, and 2.852 Å) and CH$_3$···CH (2.275 Å and 2.833 Å), were observed, which makes **TDBA-Cz** a suitable emitter for the non-doped OLEDs.

Considering the excellent photophysical properties of **TDBA-Cz**, multilayer OLEDs with an optimized device configuration of [ITO/HATCN (5 nm)/TAPC (30 nm)/TCTA (15 nm)/mCBP (10 nm)/DPEPO: x wt% **TDBA-Cz** (15 nm)/POT2T (10 nm)/ANT-BIZ (30 nm)/Liq (2 nm)/Al (100 nm)] were fabricated ($x = 10, 20, 50$), where HATCN (1,4,5,8,9,11-hexaazatriphenylenehexacarbonitrile) served as the hole-injection layer, TAPC (1,1-bis[[di-4-tolylamino)phenyl]cyclohexane) and ANT-BIZ (1-(4-(10-([1,1′-biphenyl]-4-yl)anthracen-9-yl)phenyl)-2-ethyl-1H-benzo[d]-imidazole) were employed as the hole- and electron-transport layers, respectively, while TCTA (tris(4-carbazolyl-9-ylphenyl)amine), mCBP 3,3′-di(9H-carbazol-9-yl)-1,1′-biphenyl and POT2T ((1,3,5-triazine-2,4,6-triyl)tris(benzene-3,1-diyl)(tris(diphenylphosphine oxide)) acted as exciton-blocking layers (EBL). The corresponding energy level diagram and chemical structures of the adopted materials are shown in Fig. 4. The detailed device parameters are summarized in Table 2.
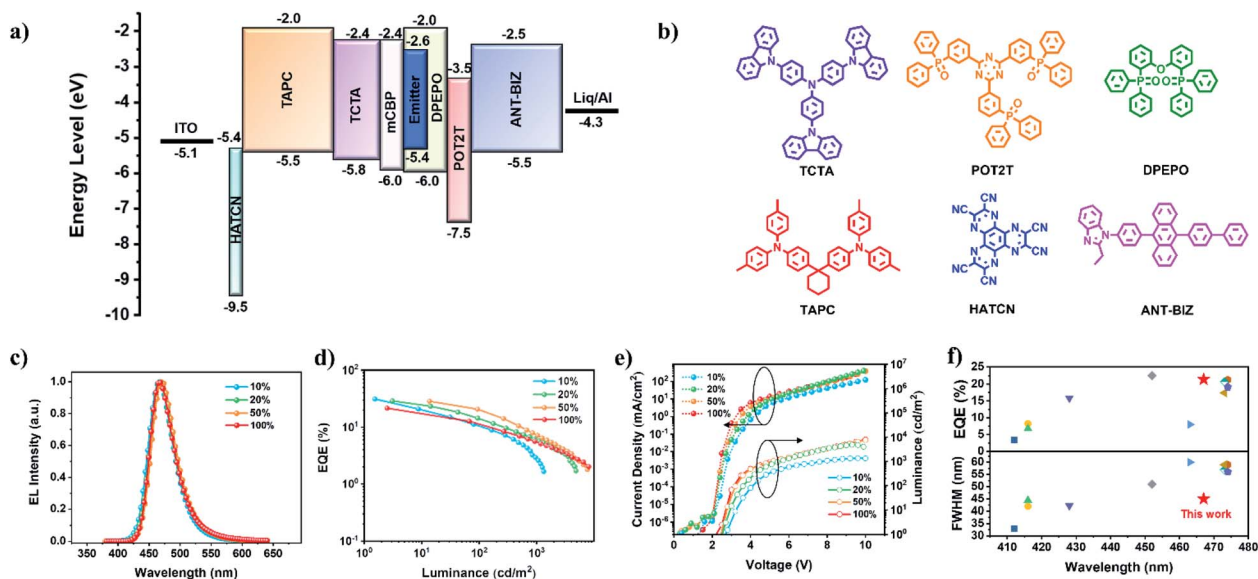
Fig. 4 (a) Device configuration and the energy level diagram. (b) Chemical structures of the materials. (c) EL spectra. (d) EQE *versus* luminance curves. (e) Current density and luminance *versus* voltage characteristics. (f) EQE and FWHM comparison of the reported non-doped blue OLEDs in the literature on the premise of FWHM less than 60 nm.

All the devices displayed a low turn-on voltage, which gradually decreased from 2.8 V to 2.6 V with the increase of the doping concentration from 10% to 50 wt%, indicating that excitons generated in the emitting layer are mainly from direct charge trapping on the guest molecules.[12] All the devices exhibited blue EL spectra and the increasing doping concentration only resulted in a slight red-shift of the emission maxima from 466 to 470 nm and an unobtrusive FWHM narrowing from 48 nm to 45 nm. The device with a 10 wt% doping concentration achieved the maximum EQE and current efficiency (CE) of up to 31.1% and 41.0 cd A^{-1} with the CIE coordinates of (0.134, 0.129), which are comparable with the reported efficiencies for the high-performance blue OLEDs.[3h,8c,13] When the doping concentration exceeded 10 wt%, the maximum EQE reduced marginally, but still maintained a maximum EQE of up to 28.4% at a doping concentration of 50%, which indicated that the highly twisted structure of **TDBA-Cz** can efficiently alleviate the concentration quenching at high doping concentrations. However for **DBA-Cz**, EL spectra showed gradual red-shifts and broadened FWHMs with the increase of doping concentration from 10 to 50 wt%, accompanied by great variations of CIE coordinates from (0.136, 0.147) to (0.147, 0.259). In addition, high EQEs of 30.3% and 29.3% were

achieved in devices with doping ratios of 10 and 20 wt%, respectively, which were comparable to those of **TDBA-Cz**, while the value dramatically dropped to 16.2% when the doping concentration increased to 50 wt% (Fig. S19 and Table S5, ESI†). In addition, compared with **DBA-Cz**, **TDBA-Cz**-based devices revealed excellent chromatic stability with minor variations of CIE coordinates within 0.03 with the increase of **TDBA-Cz** doping concentration (Fig. S20, ESI†). These results demonstrate the superiority of **TDBA-Cz** as an emitter in blue devices.

Inspired by the excellent device performances of the OLEDs at high doping concentrations, non-doped OLEDs were further fabricated with the aforementioned device configuration. As shown in Fig. 4, the turn-on voltage of the device was further dropped to 2.4 V. A slight red-shift (5 nm) of the EL spectrum could be observed compared with its PL spectrum of the neat film, accompanied by the minor FWHM broadening of only 4 nm. Remarkably, the device displayed a maximum EQE of 21.4% and CE of 31.5 cd A^{-1}, which are among the best performance values reported in blue nondoped OLEDs with the FWHM below 50 nm.[4b,8h,14] In contrast, the **DBA-Cz**-based nondoped device exhibited a relatively low efficiency with a maximum EQE of only 11.3%, which was almost half of the value for **TDBA-Cz** (Fig. S19 and Table S5, ESI†). Moreover, in

Table 2 EL performances of the TADF-OLEDs based on **TDBA-Cz**

Emitter	Dopant ratio	$V_{on}{}^a$ [V]	$\lambda_{EL}{}^b$ [nm]	FWHM^c [nm]	EQE^d [%]	CE^e [cd A^{-1}]	CIE^f (x, y)
TDBA-Cz	10%	2.8	466	47	31.1	41.0	0.134, 0.129
	20%	2.7	468	46	28.7	39.4	0.134, 0.151
	50%	2.6	470	45	28.4	38.3	0.131, 0.165
	100%	2.4	467	45	21.4	31.5	0.138, 0.155

^{a} Turn-on voltage when brightness is 1 cd m^{-2}. ^{b} Maximum EL wavelength. ^{c} FWHM of EL spectra. ^{d} Maximum EQE. ^{e} Maximum CE. ^{f} Recorded at a luminance of 1000 cd m^{-2}.

comparison with its doped device, the nondoped device of **DBA-Cz** has a slightly red-shifted emission with a maximum at 478 nm and a broadened FWHM of 63 nm, thereby resulting in poor color purity with the CIE coordinates of (0.170, 0.312). The much better EQE and CIE coordinates of **TDBA-Cz** further indicate the validity of the molecular design strategy for the nondoped device. Furthermore, the operational lifetime (LT_{50}) of these devices was evaluated at an initial luminance of 100 nit (Fig. S21, ESI†). **TDBA-Cz**-based devices exhibited lifetimes of 82.7 and 226.7 min for the doped devices with 10 wt% and 50 wt% doping concentrations, respectively, and 200.7 min for the nondoped device, all of which were longer than those of the corresponding **DBA-Cz** based devices. To date, the reported nondoped blue OLEDs with a narrow FWHM of less than 50 nm possessed an EQE_{max} less than 15.8% no matter what kinds of emitters are adopted (Table S6†). The EQE_{max} of this device is about 1.4 times as high as that of the best reported value and represents the highest EQE achieved so far (Fig. 4f). Additionally, the FWHMs of whether doped or nondoped devices are even comparable to those of the multi-resonance TADF-OLEDs. Such superior device performances can be mainly attributed to the efficient RISC process and very large SOC constants, combined with the fast k_r, k_{ISC} and k_{RISC} values.

Conclusions

In conclusion, a rational molecular design strategy for constructing highly-efficient and narrowband emission TADF emitters was demonstrated by precise peripheral decoration on the oxygen-bridged triarylboron acceptor unit. The bulky steric hindrance between the acceptor and terminal pendant endowed the compound with a highly twisted configuration, and the rigid skeleton structure resulted in an intrinsically narrow emission spectrum and extremely high PLQY whether in doped films or neat films, which is conductive to the effective suppression of concentration quenching. The nondoped blue device based on **TDBA-Cz** was achieved with a maximum EQE of 21.4%, as well as a narrow FWHM. The fine molecular modulation and the revealed structure–property relationship provide guidance for developing narrowband and high-efficiency donor–acceptor type TADF emitters.

Data availability

The datasets supporting this article have been uploaded as part of this manuscript and its corresponding ESI.† Crystallographic data can be obtained from the CCDC.

Author contributions

J. Han, J. Miao and C. Yang wrote the manuscript. J. Han and Z. Huang synthesized the compounds. J. Han measured the photophysical, thermal and electrochemical properties of the compounds. J. Miao fabricated and characterized the devices. Y. Qiu performed the temperature-dependent transient PL decay measurements. Z. Xie performed a part of the quantum

chemical calculations. C. Yang supervised the project. All authors contributed to the discussion of the results.

Conflicts of interest

There are no conflicts to declare.

Notes and references

1 (a) Y. L. Chang, Y. Song, Z. Wang, M. G. Helander, J. Qiu, L. Chai, Z. Liu, G. D. Scholes and Z. Lu, *Adv. Funct. Mater.*, 2013, **23**, 705–712; (b) S. Reineke, F. Lindner, G. Schwartz, N. Seidler, K. Walzer, B. Lüssem and K. Leo, *Nature*, 2009, **459**, 234–238; (c) B. Zhang, G. Tan, C. S. Lam, B. Yao, C. L. Ho, L. Liu, Z. Xie, W. Y. Wong, J. Ding and L. Wang, *Adv. Mater.*, 2012, **24**, 1873–1877; (d) Q. Zhang, B. Li, S. Huang, H. Nomura, H. Tanaka and C. Adachi, *Nat. Photonics*, 2014, **8**, 326–332; (e) X. Li, G. Xie, M. Liu, D. Chen, X. Cai, J. Peng, Y. Cao and S. Su, *Adv. Mater.*, 2016, **28**, 4614–4619; (f) M.-C. Tang, C.-H. Lee, M. Ng, Y.-C. Wong, M.-Y. Chan and V. W.-W. Yam, *Angew. Chem., Int. Ed.*, 2018, **57**, 5463–5466; (g) J. Kido, M. Kimura and K. Nagai, *Science*, 1995, **267**, 1332–1334; (h) B. Li, Z. Li, T. Hu, Y. Zhang, Y. Wang, Y. Yi, F. Guo and L. Zhao, *J. Mater. Chem. C*, 2018, **6**, 2351–2359; (i) R. Ishimatsu, S. Matsunami, T. Kasahara, J. Mizuno, T. Edura, C. Adachi, K. Nakano and T. Imato, *Angew. Chem., Int. Ed.*, 2014, **53**, 6993–6996; (j) X. Wang, S. Yang, Q. Tian, C. Zhong, Y. Qu, Y. Yu, Z. Jiang and L. Liao, *Angew. Chem., Int. Ed.*, 2021, **60**, 5213–5219; (k) Q. Xue and G. Xie, *Adv. Opt. Mater.*, 2021, **9**, 2002204.

2 A. Endo, K. Sato, K. Yoshimura, T. Kai, A. Kawada, H. Miyazaki and C. Adachi, *Appl. Phys. Lett.*, 2011, **98**, 083302.

3 (a) Y. Zhang, D. Zhang, J. Wei, X. Hong, Y. Lu, D. Hu, G. Li, Z. Liu, Y. Chen and L. Duan, *Angew. Chem., Int. Ed.*, 2020, **59**, 17499–17503; (b) Y. Zhang, D. Zhang, J. Wei, Z. Liu, Y. Lu and L. Duan, *Angew. Chem., Int. Ed.*, 2019, **58**, 16912–16917; (c) W. Li, B. Li, X. Cai, L. Gan, Z. Xu, W. Li, K. Liu, D. Chen and S. Su, *Angew. Chem., Int. Ed.*, 2019, **58**, 11301–11305; (d) C. Wu, W. Liu, K. Li, G. Cheng, J. Xiong, T. Teng, C.-M. Che and C. Yang, *Angew. Chem., Int. Ed.*, 2021, **60**, 3994–3998; (e) Y. Qi, W. Ning, Y. Zou, X. Cao, S. Gong and C. Yang, *Adv. Funct. Mater.*, 2021, **31**, 2102017; (f) F. Ni, C.-W. Huang, Y. Tang, Z. Chen, Y. Wu, S. Xia, X. Cao, J.-H. Hsu, W.-K. Lee, K. Zheng, Z. Huang, C.-C. Wu and C. Yang, *Mater. Horiz.*, 2021, **8**, 547–555; (g) N. Li, D. Chai,

Z. Chen, C. Zhou, F. Ni, Z. Huang, X. Cao, G. Xie, K. Li and C. Yang, *Chem. Eng. J.*, 2020, **396**, 125276; (*h*) H. Lim, H. J. Cheon, S.-J. Woo, S.-K. Kwon, Y.-H. Kim and J.-J. Kim, *Adv. Mater.*, 2020, **32**, 2004083; (*i*) H. Liu, Z. Liu, G. Li, H. Huang, C. Zhou, Z. Wang and C. Yang, *Angew. Chem., Int. Ed.*, 2021, **60**, 12376–12380.

4 (*a*) J. U. Kim, I. S. Park, C.-Y. Chan, M. Tanaka, Y. Tsuchiya, H. Nakanotani and C. Adachi, *Nat. Commun.*, 2020, **11**, 1765; (*b*) I. S. Park, K. Matsuo, N. Aizawa and T. Yasuda, *Adv. Funct. Mater.*, 2018, **28**, 1802031; (*c*) M. Yang, I. S. Park and T. Yasuda, *J. Am. Chem. Soc.*, 2020, **142**, 19468–19472; (*d*) D. Karthik, Y. H. Jung, H. Lee, S. Hwang, B.-M. Seo, J.-Y. Kim, C. W. Han and J. H. Kwon, *Adv. Mater.*, 2021, **33**, 2007724; (*e*) H. Hirai, K. Nakajima, S. Nakatsuka, K. Shiren, J. Ni, S. Nomura, T. Ikuta and T. Hatakeyama, *Angew. Chem., Int. Ed.*, 2015, **54**, 13581–13585; (*f*) D. Song, Y. Yu, L. Yue, D. Zhong, Y. Zhang, X. Yang, Y. Sun, G. Zhou and Z. Wu, *J. Mater. Chem. C*, 2019, **7**, 11953–11963; (*g*) X. Zheng, R. Huang, C. Zhong, G. Xie, W. Ning, M. Huang, F. Ni, F. B. Dias and C. Yang, *Adv. Sci.*, 2020, **7**, 1902087.

5 (*a*) M. Godumala, S. Choi, M. J. Cho and D. H. Choi, *J. Mater. Chem. C*, 2019, **7**, 2172–2198; (*b*) K. Wu, T. Zhang, Z. Wang, L. Wang, L. Zhan, S. Gong, C. Zhong, Z.-H. Lu, S. Zhang and C. Yang, *J. Am. Chem. Soc.*, 2018, **140**, 8877–8886; (*c*) S. J. Yoon, J. H. Kim, W. J. Chung and J. Y. Lee, *Chem.–Eur. J.*, 2021, **27**, 3065–3073; (*d*) Y. Gao, W. Guan, L. Yan and Z. Su, *J. Mater. Chem. C*, 2020, **8**, 219–227; (*e*) B. Du, X. Wang, F. Chen, Q. Yang, S. Shao, L. Wang, X. Jing and F. Wang, *Chem. Commun.*, 2021, **57**, 7144–7147.

6 Y. J. Cho, S. K. Jeon, S.-S. Lee, E. Yu and J. Y. Lee, *Chem. Mater.*, 2016, **28**, 5400–5405.

7 T. Hatakeyama, K. Shiren, K. Nakajima, S. Nomura, S. Nakatsuka, K. Kinoshita, J. Ni, Y. Ono and T. Ikuta, *Adv. Mater.*, 2016, **28**, 2777–2781.

8 (*a*) Y. Im, S. H. Han and J. Y. Lee, *J. Mater. Chem. C*, 2018, **6**, 5012–5017; (*b*) Y. J. Cho, S. K. Jeon and J. Y. Lee, *Adv. Opt. Mater.*, 2016, **4**, 688–693; (*c*) Y. H. Lee, S. Park, J. Oh, S.-J. Woo, A. Kumar, J.-J. Kim, J. Jung, S. Yoo and M. H. Lee, *Adv. Opt. Mater.*, 2018, **6**, 1800385; (*d*) Y. J. Cho, B. D. Chin, S. K. Jeon and J. Y. Lee, *Adv. Funct. Mater.*, 2015, **25**, 6786–6792; (*e*) D. R. Lee, M. Kim, S. K. Jeon, S.-H. Hwang, C. W. Lee and J. Y. Lee, *Adv. Mater.*, 2015, **27**, 5861–5867; (*f*) M. Kim, S. K. Jeon, S.-H. Hwang and J. Y. Lee, *Adv. Mater.*, 2016, **28**, 603; (*g*) H. L. Lee, K. H. Lee,

J. Y. Lee and W. P. Hong, *J. Mater. Chem. C*, 2019, **7**, 6465–6474; (*h*) X. Chen, J. Jia, R. Yu, J. Liao, M. Yang and C. Lu, *Angew. Chem., Int. Ed.*, 2017, **56**, 15006–15009; (*i*) Z. Zhang, E. Crovini, P. L. dos Santos, B. A. Naqvi, D. B. Cordes, A. M. Z. Slawin, P. Sahay, W. Brutting, I. D. W. Samuel, S. Brase and E. Zysman-Colman, *Adv. Opt. Mater.*, 2020, **8**, 2001354; (*j*) X. Liang, Z. Yan, H. Han, Z. Wu, Y. Zheng, H. Meng, J. Zuo and W. Huang, *Angew. Chem., Int. Ed.*, 2018, **57**, 11316–11320.

9 G. Meng, X. Chen, X. Wang, N. Wang, T. Peng and S. Wang, *Adv. Opt. Mater.*, 2019, **7**, 1900130.

10 (*a*) F. Liu, H. Liu, X. Tang, S. Ren, X. He, J. Li, C. Du, Z. Feng and P. Lu, *Nano Energy*, 2020, **68**, 104325; (*b*) D. H. Ahn, H. Lee, S. W. Kim, D. Karthik, J. Lee, H. Jeong, J. Y. Lee and J. H. Kwon, *ACS Appl. Mater. Interfaces*, 2019, **11**, 14909–14916; (*c*) W. Song, I. Lee and J. Y. Lee, *Adv. Mater.*, 2015, **27**, 4358–4363.

11 Y. K. Chen, J. Jayakumar, C. M. Hsieh, T. L. Wu, C. C. Liao, J. Pandidurai, C. L. Ko, W. Y. Hung and C. H. Cheng, *Adv. Mater.*, 2021, **33**, 2008032.

12 H. Kaji, H. Suzuki, T. Fukushima, K. Shizu, K. Suzuki, S. Kubo, T. Komino, H. Oiwa, F. Suzuki, A. Wakamiya, Y. Murata and C. Adachi, *Nat. Commun.*, 2015, **6**, 8476.

13 (*a*) K. Suzuki, S. Kubo, K. Shizu, T. Fukushima, A. Wakamiya, Y. Murata, C. Adachi and H. Kaji, *Angew. Chem., Int. Ed.*, 2015, **54**, 15231–15235; (*b*) P. Ganesan, D.-G. Chen, W.-C. Chen, P. Gnanasekaran, J.-A. Lin, C.-Y. Huang, M.-C. Chen, C.-S. Lee, P.-T. Chou and Y. Chi, *J. Mater. Chem. C*, 2020, **8**, 4780–4788; (*c*) Y. H. Lee, S. Park, J. Oh, J. W. Shin, J. Jung, S. Yoo and M. H. Lee, *ACS Appl. Mater. Interfaces*, 2017, **9**, 24035–24042; (*d*) I. S. Park, M. Numata, C. Adachi and T. Yasuda, *Bull. Chem. Soc. Jpn.*, 2016, **89**, 375–377.

14 (*a*) I. S. Park, K. Matsuo, N. Aizawa, T. Yasuda, S. H. Park, C. W. Koh, C. W. Kim, H. Y. Woo, M. J. Cho, S. Park and D. H. Choi, *Adv. Funct. Mater.*, 2018, **28**, 1802031; (*b*) J. Hwang, H. Kang, J.-E. Jeong, H. Y. Woo, M. J. Cho, S. Park and D. H. Choi, *Chem. Eng. J.*, 2021, **416**, 129185; (*c*) S. Zou, F. Xie, M. Xie, Y. Li, T. Cheng, X. Zhang, C.-S. Lee and J. Tang, *Adv. Sci.*, 2020, **7**, 1902508; (*d*) K. Matsuo and T. Yasuda, *Chem. Sci.*, 2019, **10**, 10687–10697; (*e*) C. Li, Z. Ren, X. Sun, H. Li and S. Yan, *Macromolecules*, 2019, **52**, 2296–2303.